Paleoceanography and Paleoclimatology®

RESEARCH ARTICLE
10.1029/2024PA004897

Key Points:

- We present a machine learning method to quantify iceberg rafted debris (IRD) in deep-sea sediment cores
- We quantify IRD at three International Ocean Discovery Program sites in the heart of Iceberg Alley over 3.3 million years
- We propose that Antarctica transitions from a primarily terrestrial-terminating to marine-terminating ice sheet 1.8 million years ago

Supporting Information:

Supporting Information may be found in the online version of this article.

Correspondence to:
C. E. Jasper,
cjasper@ldeo.columbia.edu

Citation:
Jasper, C. E., Dyer, B., Reilly, B. T., Williams, T., Hemming, S., & Raymo, M. E. (2024). A 3.3-million-year record of Antarctic iceberg rafted debris and ice sheet evolution quantified by machine learning. *Paleoceanography and Paleoclimatology*, *39*, e2024PA004897. https://doi.org/10.1029/2024PA004897

Received 19 MAR 2024
Accepted 9 AUG 2024

A 3.3-Million-Year Record of Antarctic Iceberg Rafted Debris and Ice Sheet Evolution Quantified by Machine Learning

Claire E. Jasper[1,2], Blake Dyer[3], Brendan T. Reilly[1], Trevor Williams[4], Sidney Hemming[1], and Maureen E. Raymo[1]

[1]Lamont-Doherty Earth Observatory, Columbia University, Palisades, NY, USA, [2]Department of Earth and Environmental Sciences, Columbia University, New York, NY, USA, [3]School of Earth and Ocean Sciences, University of Victoria, Victoria, BC, Canada, [4]International Ocean Discovery Program, Texas A&M University, College Station, TX, USA

Abstract Over the last 3.3 million years, the Antarctic Ice Sheet (AIS) has undergone phases of ice sheet growth and decay, impacting sea level and climate globally. Presently, the largely marine-terminating AIS loses mass primarily by iceberg calving and basal melt of ice shelves. Quantifying past rates and timing of AIS melt is vital to understanding future cryosphere and sea level changes. One proxy for past ice sheet instabilities is iceberg rafted debris (IRD) fluxes. However, traditional methods of IRD quantification are labor-intensive. Here, we present a new method of identifying IRD grains in sediment core X-ray images using a convolutional neural network machine learning algorithm. We present a 3.3-million-year record of AIS IRD melt events using sediment cores from International Ocean Discovery Program Sites U1536, U1537, and U1538 in the Southern Ocean's "Iceberg Alley." We identify two increases in the IRD fluxes throughout this period, at ∼1.8 and 0.43 Ma. We propose that after 1.8 Ma, the AIS expanded and transitioned from a primarily terrestrial-terminating to a primarily marine-terminating ice sheet. Therefore, after 1.8 Ma, glacial terminations and AIS iceberg discharge are associated with variations in global ice volume, presumably through the mechanism of sea level and, therefore, grounding line change. The second AIS regime change occurs during the Mid-Brunhes Event (∼0.43 Ma). After this time, there are heightened and continuous IRD fluxes at each glacial termination, indicating increased AIS size and instability after this time.

Plain Language Summary Understanding the timing and magnitude of the melt and retreat of the Antarctic Ice Sheet (AIS) in the past can help us understand its sensitivity to future global climate change. One way to understand ice sheets in the past is to identify and quantify sand to pebble-sized rock and mineral grains incorporated into ice sheets and exported to the ocean by icebergs. These so-called iceberg rafted debris (IRD) grains get deposited on the seafloor when icebergs melt, and they are easily identifiable in deep-sea sediment core X-ray images. Here, we present an artificial intelligence image detection method to identify IRD in sediment cores collected in the heart of "Iceberg Alley," a region that today receives the majority of Antarctic icebergs. We find that over the past 3.3 million years, there have been two increases in the amount of IRD deposited. We propose that the first major increase in IRD just after 1.8 Ma is evidence of an expansion of the AIS to an ice sheet with marine margins and ice shelves. We further propose that after 430,000 years ago, the AIS undergoes additional expansion and sees consistent, rapid retreat at the end of each global glaciation.

1. Introduction

During the late Cenozoic, Earth's ice sheets waxed and waned on millennial to million-year timescales (e.g., Hays et al., 1976; Hodell et al., 2023). Understanding the timing and causes of past ice sheet evolution is vital to refining sea level projections for the 21st century. Currently, parts of East Antarctica are gaining mass while most of West Antarctica is losing mass (as observed by GRACE and GRACE-FO; Tapley et al., 2019). How these trends will play out over the coming few centuries remains uncertain. Global records of ice volume from benthic foraminiferal δ^{18}O broadly indicate when periods of globally integrated ice sheet growth and decay occurred (Lisiecki & Raymo, 2005). However, sediment records near ice sheets can provide a more detailed and nuanced view of the individual ice sheet and catchment dynamics at each pole.

As ice sheets flow across landscapes, they erode continental rock and incorporate it into their mass (Alley et al., 1997). When marine-terminating glaciers calve into the ocean, the resulting icebergs transport the terrigenous material they carry until it melts out and is deposited on the ocean floor, both in proximal and distal marine locations. As these icebergs melt, the material they carry, so-called "iceberg rafted debris" (IRD), gets deposited in the deep ocean. Although IRD spans all grain sizes, we count the larger grains (typically >150 microns) as a proxy for IRD deposition because they are uniquely carried by icebergs, rather than by bottom currents or wind (Andrews, 2000; Ruddiman, 1977). Quantifying the timing and pacing of large IRD events can yield insights into the magnitude, pacing, and cyclicity of icebergs and, therefore, ice sheet dynamics.

The export of Antarctic IRD to the deep ocean depends on two main factors: ice sheet dynamics and the extent of cold surface water masses that allow icebergs to survive at sea (Diekmann et al., 2003). During interglacial periods, icebergs calving off Antarctica deposit IRD near the continent, with fluxes decreasing northward as icebergs encounter warmer water (Keany et al., 1976). Conversely, during glacial periods, IRD deposition extends to more northern latitudes, likely because of the northward movement of the 0°C isotherm, more extensive sea ice, and changes in ocean circulation (Starr et al., 2021; Teitler et al., 2010). Antarctic IRD maxima at sites near the continent are interpreted as the consequence of accelerated calving during the retreat of marine-terminating outlet glaciers (e.g., Bailey et al., 2022; Cowan, 2001; Passchier, 2011; Patterson et al., 2014; Weber et al., 2014; Williams et al., 2010; Wilson et al., 2018). It has also been suggested that Antarctic Ice Sheet (AIS) grounding line retreat and mass loss can be accelerated by local sea-level rise caused by northern hemisphere (NH) ice sheet melt (Denton et al., 1986; Gomez et al., 2020; Raymo et al., 2006).

Historically, IRD records from the North Atlantic were quantified by hand-counting sediment grains in sieved samples because of the presence of foraminifera in the sand fraction (e.g., Barker et al., 2022; McManus et al., 1999; Raymo et al., 1986). However, since the Southern Ocean has low carbonate preservation (Diekmann, 2007), Antarctic IRD records are generally measured by either weighing the sand fraction (e.g., Passchier, 2011; Patterson et al., 2014; Williams et al., 2010) or manually counting visible grains in sediment core X-ray images (Cowan et al., 2008; Grobe, 1987; Weber et al., 2014). Recent work by McKay et al. (2022) illustrates the comparable results of counting IRD in X-ray images and weighing IRD in the sand fraction for Antarctic-proximal sediment cores. While all of these methods of IRD quantification give robust and comparable results, manually counting IRD is well-known to be labor-intensive. In addition, recent work has automated the counting of IRD in 3-D X-Ray computed tomography (CT) images by thresholding the IRD grains by density, an advantage of 3-D images versus 2-D X-ray images (Bartels et al., 2017; Cederstrøm et al., 2021; Reilly et al., 2019). However, full 3-D CT images of each section of long drill cores, such as those collected by the International Ocean Discovery Program (IODP), are not standard shipboard measurements.

Here we present a new methodology for efficiently identifying and quantifying IRD grains in standard shipboard 2-D X-ray images of IODP sediment drill cores via a computer vision artificial intelligence (AI) algorithm. Specifically, we have built and trained a convolutional neural network (CNN), which is an algorithm demonstrated to be capable of differentiating objects in 2D imagery (Krizhevsky et al., 2012; LeCun et al., 2010). CNNs are computer vision models used in many repetitive image-detection tasks. To differentiate objects, the neural network learns to identify relatively complex visual features, such as edges, gradients, and textures. The algorithm learns these patterns from a training set of images that have been labeled manually by a human. This subset of training images is then fed into the CNN. Once the CNN has been trained over a series of iterations (called epochs), the CNN model can be used to identify features in unseen images. AI image detection and segmentation algorithms (like CNNs) have been widely used with X-rays in the medical field to detect health abnormalities (Habib et al., 2020; Wang et al., 2020), and their popularity is growing in the geosciences (e.g., Chaipornkaew et al., 2022; Lai et al., 2020; Marchant et al., 2020). However, their application to the thousands of deep-sea sediment core X-ray images is as of yet underexplored. Here we use a CNN to quantify the flux of IRD from IODP Expedition 382 Sites in the Scotia Sea for the past 3.3 Ma.

2. Materials and Methods

2.1. Iceberg Alley

International Ocean Discovery Program (IODP) Expedition 382 drilled three sites (U1536–U1538) in the Scotia Sea, in the Atlantic Ocean sector of the Southern Ocean (Figure 1; Weber et al., 2019). This expedition recovered two high-resolution records of late Pliocene and Pleistocene sedimentation at Sites U1536 and U1537 within the

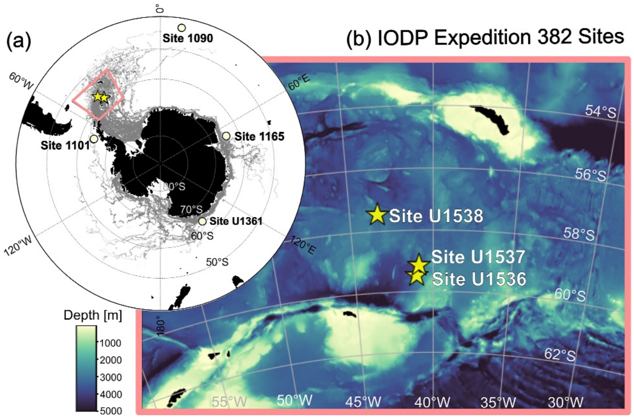

Figure 1. Map of study region. (a) Map of Antarctica with satellite-derived iceberg (>5 km) tracks from 1992 to 2022 in gray from the BYU Antarctic Iceberg Tracking Database (Stuart & Long, 2011). Location of IODP Sites U1536, U1537, and U1538 marked as yellow stars. Location of other ODP/IODP Sites relevant to this study marked as light yellow circles. Pink box from (a) is the region highlighted in panel (b). Zoom in map in panel (b) shows local bathymetry around IODP Sites U1536, U1537, and U1538. Bathymetry from GEBCO (https://www.gebco.net/). ODP, Ocean Drilling Program. IODP, International Ocean Discovery Program.

Dove Basin and one at Site U1538 in the Pirie Basin (Figure 1b). The Dove and Pirie Basins are situated just north of a major iceberg export pathway, colloquially known as "Iceberg Alley" (Figure 1a; Anderson & Andrews, 1999). The majority of icebergs that calve off Antarctica get caught in the near-shore Antarctic Coastal Current and are transported counter-clockwise (Stuart & Long, 2011). When icebergs reach the east side of the Antarctic Peninsula, they deflect northward within the Weddell Gyre. Once north of the Antarctic Peninsula, the icebergs are entrained in the eastward-flowing Antarctic Circumpolar Current (ACC), a warmer current that melts the icebergs, depositing their IRD on the seafloor (Silva et al., 2006).

Modern satellite observations of large, tabular icebergs show that the majority of icebergs exported from the Weddell Gyre are sourced from the Filchner-Ronne Ice Shelf as well as East Antarctic Ice Sheet (EAIS) catchments (Figure 1a; Stuart & Long, 2011). However, iceberg trajectory modeling work shows that the size of Antarctic icebergs could affect the trajectory, with the majority of icebergs moving along the western edge of the Weddell gyre and a secondary, minor group of smaller-sized icebergs deflecting northward toward the ACC further east of the classic "Iceberg Alley" (Rackow et al., 2017). In addition, iceberg trajectories during the past were likely different from today (Starr et al., 2021), and there is evidence from IODP Site U1538 in the Pirie Basin of icebergs sourced from the West Antarctic Ice Sheet (WAIS) at 1.2 Ma (Bailey et al., 2022). Therefore, when discussing the flux of IRD at Sites U1536, U1537, and U1538 over the past 3.3 Ma, we remain agnostic to the source of the icebergs (EAIS or WAIS) and thus henceforth say AIS iceberg discharge when discussing our IRD fluxes.

2.2. Drill Sites and Age Model

The sediments from Sites U1536 and U1537 are part of a ~1 km thick contourite deposit in the northeast section of Dove Basin. Site U1536 (59°26.46′S, 41°3.66′W) was drilled in 3,220 m of water 235 km northeast of the South Orkney Islands, and Site U1537 (59°6.65′S, 40°54.37′W) was drilled northeast of U1536 in 3,713 m water depth (Weber et al., 2019). In the Dove Basin, the contouritic fine-grained silt and clay are deposited from the eastward flow pathway of the Antarctic Circumpolar Current as well as from the northward flowing Weddell Sea Deep Water (Huang et al., 2020; Maldonado et al., 2003; Naveira Garabato et al., 2002). This fine-grained silt and clay deposited at these sites is smaller than the typical grain size that defines IRD (>150 μm). Therefore, quantifying IRD in contourite drifts is common because contourites have high sedimentation rates, which are ideal for high temporal resolution, and the uniformly fine-grained silt and clay sediments of contourites are ideal for the identification of the poorly-sorted IRD grains. For the Dove Basin drill sites, sedimentation rates range from ~5 to 20 cm per thousand years (Reilly et al., 2021). Paleomagnetic polarity zones were measured throughout Sites U1536 and U1537. The Site U1537 Advanced Piston Core/Half-Length Advanced Piston Core (APC/HLAPC) sections of the site extend continuously to at least the late Gilbert Subchron (>3.6 Ma). However, there are slumped sedimentary intervals below the base of the Mammoth Subchron (3.33 Ma; Weber et al., 2021). There is also a slump in Site U1537 from 209.5 to 214 m core composite depth below the seafloor (m CCSF), which is well-constrained between age tie points at ~1.675 Ma (Weber et al., 2021). The Site U1536 APC/HLAPC splice goes to the lower Gauss Chron (3.6 Ma) and is nearly continuous except for two slumps in the late Pleistocene at 54.9–60.2 m CCSF and at 92.97–102.5 m CCSF (Weber et al., 2021).

The age model applied to Sites U1536 and U1537 combines two previously published age models (Reilly et al., 2021; Weber et al., 2022) using the MATLAB *Undatable* software (Lougheed & Obrochta, 2019). For the 0–1.5 Myr interval, Weber et al. (2022) show evidence that the amplitude and variability of the Site U1537 magnetic susceptibility matches the EPICA Dome C dust fluxes and the LR04 benthic foraminiferal oxygen isotope stack (Bazin et al., 2013; Lisiecki & Raymo, 2005). Between 1.5 and 1.78 Ma, we use the last tie from Weber et al. (2022) and the Upper Olduvai reversal as age control points. For intervals older than 1.78 Ma, we rely on the magnetostratigraphic age model in Reilly et al. (2021). This age model captures all major reversals through the late Pliocene and Pleistocene and assumes a linear sedimentation rate between reversals (Tables S1 and S2 in

Supporting Information S2). We apply this age model to Site U1536 by using the U1536/U1537 depth correlation in Reilly et al. (2021).

In addition to the Dove Basin sites, IODP Expedition 382 recovered a Pleistocene sedimentary record at Site U1538 (57°26.5248′S 43°21.4691′W) in the northern Pirie Basin in 3,131 m water depth (Figure 1b; Weber et al., 2019). Site U1538 is further north than the two Dove Basin sites. The spliced Site U1538 record is only continuous down to 124 m CCSF, to Marine Isotope Stage (MIS) 12 (478 ka). Bailey et al. (2022) finds that the amplitude and variability of Site U1538 (Pirie Basin) physical properties, such as natural gamma radiation (NGR), correlate strongly with the Dove Basin physical properties. Therefore, the spliced Site U1538 record was correlated to the Dove Basin stack (Reilly et al., 2021) using NGR (Table S3 in Supporting Information S2, following Bailey et al., 2022). We then extend the age model beyond the splice down Hole U1538A by correlating the core depth below sea floor (CSF-A) of Hole U1538A to the Dove Basin stack (Reilly et al., 2021) following Bailey et al. (2022).

2.3. Data Preparation

During IODP Expedition 382, the archive halves of the Sites U1536–U1538 sediment cores were scanned stepwise on a passthrough X-Ray Imager (XRI), which is composed of two units: a Teledyne ICM CP120B X-Ray generator and a detector unit that consists of a Go-Scan 1510 H system with an array of CMOS sensors. The detector has an active area of 10.2 × 15.3 cm and a resolution of 99 µm. The half sections were measured on the XRI at 12 cm intervals. Each 12 cm interval yielded an X-ray image 15 cm long, including 3 cm of overlap between X-ray images.

See the Methods section in Weber et al. (2021) for more details.

The raw 16-bit X-ray images have low contrast (Figure 2a), so we employ two steps to enhance each image. Since the center of the core half-round is equal to the radius of the core barrel and the X-ray generator must penetrate more material at the center of the half-core than at the edges the raw images appear darker in the center and lighter near the edges. We correct this bias by subtracting pixel brightness values based on the *x*-axis values of the images (Figure 2b), which normalizes them by darkening the cores' edges and brightening their centers. Then, the bias-corrected images are contrast-enhanced (Figure 2c) using Scikit-image Contrast Limited Adaptative Histogram Equalization (van der Walt et al., 2014). This algorithm outputs a high-contrast image with features like IRD and pyritized burrows sharpened and darkened. This enhancement algorithm was chosen because it enhances images based on histograms over smaller sections of the image which therfore enhances full images better than a basic contrast increase. The shipboard X-ray image contrast was completed using the IODP "in-house" Processing Utility in the Integrated Measurement System (IMS) software v. 10.3 (Weber et al., 2019). Although the IMS software batch enhanced X-ray images, we found that the Scikit-image Contrast Limited Adaptive Histogram Equalization enhances each X-ray image in more detail. This step is instantaneous in the workflow, as it is applied before the image is input into the CNN. After these enhancement steps, a subset of these X-ray images were used for the CNN training set.

2.4. Training Set Construction

IRD is identifiable within the enhanced X-ray images as very coarse sand to pebble-sized black shapes. The CNN training set was built using X-ray images from Sites U1536 and U1537. Images were chosen based on the diversity of core features, including high and low IRD density, burrows (Figure S1a in Supporting Information S1), and core disturbance features, including cracks (Figure S1b in Supporting Information S1) and X-ray imaging artifacts (Figures S1c and S1d in Supporting Information S1). Images were loaded into Photoshop, and vectorized shapes were drawn around each IRD grain to generate a training set labeled with the *Y*-*X* location and shape of each IRD grain (Figure 2d). We also labeled a training set of non-IRD features that were initially misidentified as IRD by the CNN. Specifically, the cores have an abundance of pyritized burrows that are visible as long black (dense) thread-like shapes with sharp edges, which in early CNN training iterations were erroneously identified as IRD. To allow the training set to differentiate these features, a subset of images with these confounding features were labeled as "non-IRD features."

The final training set was created by making small 128 × 128-pixel grayscale image "tiles" from the original labeled full-size X-ray images (Figure 2e). The training set has two classes of training tiles: a class of tiles with an

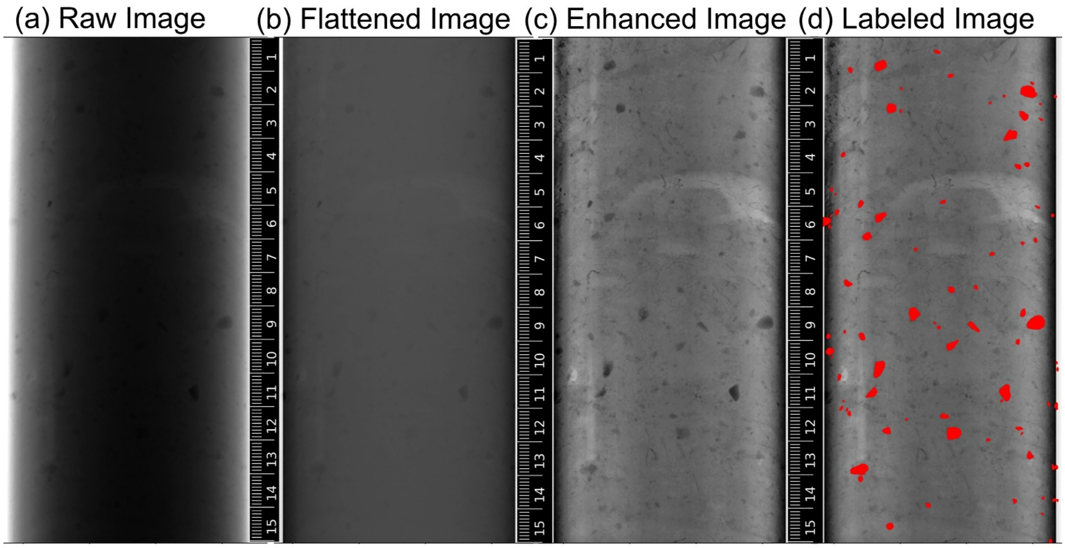

(e) Training tiles for convolutional neural network

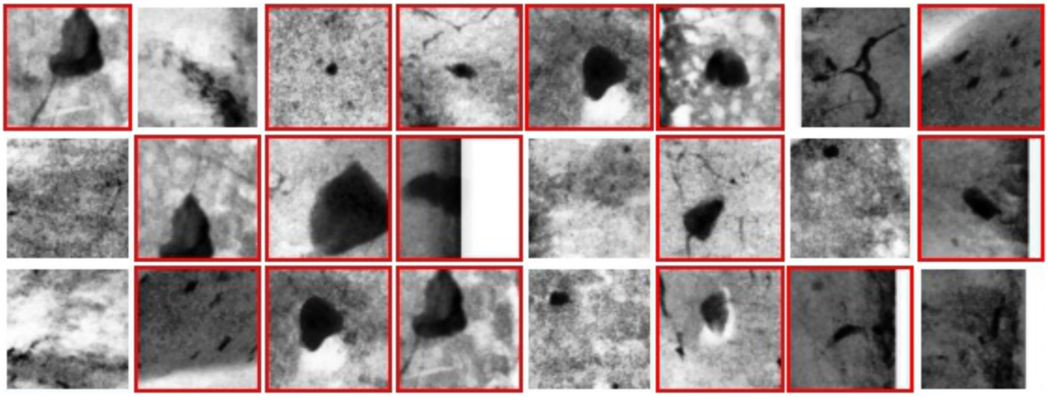

Figure 2. Image processing steps and training set creation. (a) Example of a 16-bit, 15-cm raw X-ray image from the pass-through X-Ray Imager. (b) A "flatten" function is applied to the raw X-ray image so that the geometry of the core does not interfere with the brightness contrast of the image. (c) The flattened X-ray image is then enhanced using the Scikit-image Contrast Limited Adaptative Histogram Equalization. (d) Red polygons are then drawn over the IRD grains, which labels them in the image. (e) The labeled image is then broken up into a series of 128 × 128-pixel square training "tiles." Tiles with a red border are training images with an IRD grain at the center pixel. Tiles without a red border are training images that do not have IRD grains at the center pixel. Note, some of these "non-IRD" training images have targeted features such as pyritized burrows (in the top right). IRD, iceberg rafted debris.

IRD as the center pixel and the second class where the center pixel is not IRD. In total, we trained the CNN on 70,000 of these 128 × 128-pixel training tiles: 35,000 tiles with IRD and 35,000 tiles with other features, including X-ray imaging artifacts, burrows, edges, and sedimentological disturbances. This training set should be robust and useable by others for their own IRD identification. However, additional testing on new images is recommended before the model is applied. For example, if there are other confounding features not in this training set or if the shape/size of IRD is different, then a new training set would need to be developed, and the model would need to be re-trained.

2.5. Convolutional Neural Network Architecture

The 10-layer CNN architecture presented here is based on the model by Dyer et al. (2021) (Figure S2 in Supporting Information S1), which uses the Keras Application Programming Interface within a TensorFlow framework (Abadi et al., 2015; Chollet, 2015). We also added a data augmentation generator that randomly rotates the training tiles orthogonally and/or flips them horizontally or vertically each time they are seen by the

CNN—manipulations that increase the diversity and effective size of the training set. A thorough description of our CNN can be found in our Supporting Information S1.

2.6. Labeling IRD Grains at IODP Sites U1536, U1537, and U1538

The trained CNN was then applied to IODP Expedition 382 X-ray images. Since the XRI pixel resolution is 99 μm, we only quantify IRD grains with major axis length ≥1 mm, which equates to ∼10 pixels. To calculate a consistent flux and avoid sediment core edge effects, we label the center 550 pixels (i.e., 5.5 cm) of each image (Figures 3d and 3f). In addition, we do not label the top and bottom cm of each X-ray image since there is a 3 cm overlap, and the additional overlap is deleted when we assign depth downcore.

We labeled all images of the extended splices from Site U1536 until Section 382-U1536A-52F-2 (304.76 m CCSF-A) and Site U1537 until the bottom of Core 382-U1537D-36F, 309 m CCSF-A, below which sedimentary slumps are observed as inclined or disturbed beds from Cores 382-U1537D-37F through 50F (Reilly et al., 2021; Weber et al., 2021). For Site U1538, we labeled X-ray images of the splice down to the bottom of Core 382-U1538A-14H (134 m CCSF-A) and then of only Hole U1538A down to Core 382-U1538A-31F (288 m CSF-A). For images of Hole U1538A labeled below the splice, the top of each core X-ray image was inspected for drilling disturbance and evidence of IRD "fall-in" from the drill hole sidewalls, and a "top offset" was assigned to avoid these disturbances (Table S4 in Supporting Information S2). We also added "top offsets" at Sites U1536 and U1537 for cores part of the Reilly et al. (2021) extended splice (Tables S5 and S6 in Supporting Information S2).

The labeled output X-ray images then get read into a code where the IRD-labeled pixels then get combined into shapes using the Python image processing package scikit-image (van der Walt et al., 2014). These shapes then get assigned a *Y*-axis location down the image, and that *Y*-axis location is then correlated to the depth in the sediment core section, which is then correlated to the CCSF-A depth, and then age. We can then bin the IRD counts into 1 or 5 kyr bins and divide by the area of the half-round core to get IRD flux.

2.7. Groundtruthing CNN-Labeled IRD Counts and Human Eye Counts

We compared CNN-labeled IRD counts to human IRD counts. During IODP Expedition 382, scientists on both the day and night shifts identified IRD grains ≥1 mm in a series of X-ray images that were contrast-enhanced shipboard from a 550 cm interval in Core U1536A-2H (Table S7 in Supporting Information S2; Weber et al., 2021). The scientists placed a 1 × 1 mm grid over each X-ray image and counted each IRD grain in centimeter depth intervals. If an IRD grain crossed a centimeter line, it was counted in the centimeter interval where the large portion of the grain was located. We generally observe good inter-shift correlation of IRD counts within the same depth interval—hereafter called shipboard eye counts 1 and 2 (Figure 3a). Shipboard eye counts 1 and 2 align between 8 and 9.5 m CSF-A and between 11 and 12.5 m CSF-A. However, shipboard eye counts diverge between 9.5 and 10 m CSF-A, where shipboard eye counts 1 observed 22 to 23 IRD grains per cm, and shipboard eye count 2 observed 6 to 7 IRD grains per cm (Figure 3a).

If we compare the human eye counts to the CNN counts, we find that the CNN identifies a similar range of IRD to the human eye on the cm-to-cm scale (Figure 3b). For example, at ∼9.16 m CSF-A, where shipboard eye counts 1 and 2 observe 20 IRD grains per cm, the CNN also identifies 20 IRD grains. We bin the IRD counts into 1-, 5-, and 10-cm intervals and compute the Pearson correlation coefficient and p-value between CNN-labeled IRD grain counts and the two shipboard eye counts at these various bin widths (Figure S3c in Supporting Information S1). For the 1-cm bins, we find that the correlation between shipboard eye counts 1 and 2 and the CNN-labeled counts ranges between 0.319 and 0.434 (p-value < 0.05). We suggest that this relatively low correlation is likely due to slight differences in the exact cm counted (Figure S3a in Supporting Information S1). When binned at 5-cm intervals, shipboard eye counts 1 and 2 have a correlation of 0.555, whereas each shipboard eye count (1 or 2) versus the CNN-labeled count has a correlation of 0.582 and 0.593, respectively (Figure S3b in Supporting Information S1). Correlations increase when we increase the bin size to 10 cm, where shipboard eye counts 1 and 2 have a correlation of 0.7, and each shipboard eye count (1 or 2) versus the CNN-labeled counts has a correlation of 0.611 and 0.717, respectively (Figures 3d–3f). We also note that correlations between human eye counts and CNN counts plot slightly above the 1:1 line, suggesting that the human eye was identifying more IRD than the CNN. This offset is likely because the CNN does not identify IRD on the edges of the cores (to ensure consistent flux volume). Overall, the CNN performs quite well compared to shipboard eye counts 1 and 2, with the resulting correlation always within a 10% range of correlation coefficients. As such, CNN-labeled counts are within the error and variability of human

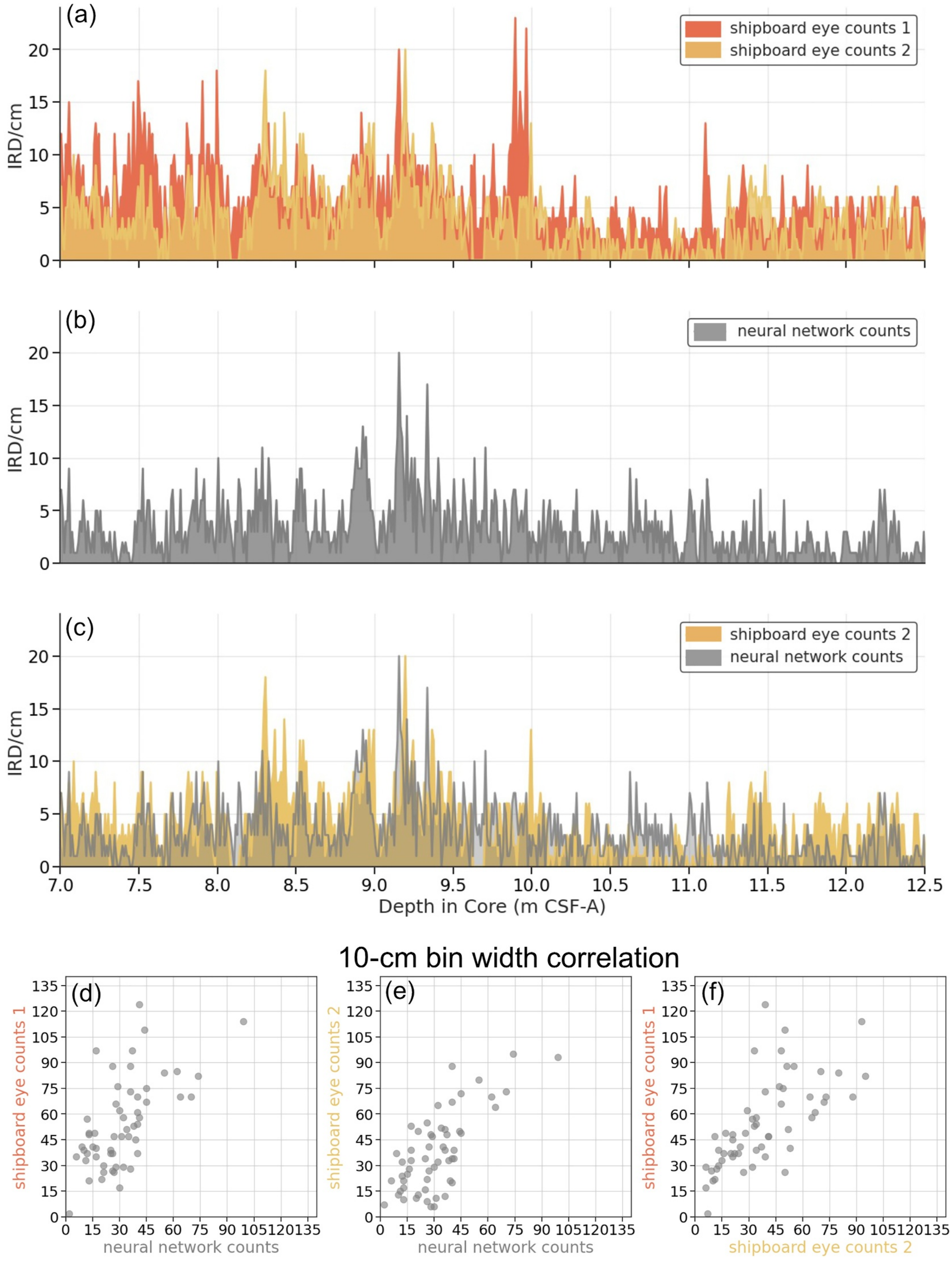

Figure 3. Ground truth of convolutional neural network to human eye counts. (a) Shipboard human eye counts of iceberg rafted debris (IRD) ≥1 mm in each centimeter of Core 382-U1536C-2H X-ray images from 7.0 to 12.5 m CSF-A by two different groups, shipboard eye counts 1 (orange) and shipboard eye counts 2 (yellow). (b) The CNN-labeled IRD counts (gray) for grains ≥1 mm over the same interval as (a). (c) Shipboard eye counts 2 (yellow) overlayed over the CNN-labeled IRD counts (gray) as a visual representation of the similarity of the neural network and human eye counts. (d–f) Correlation plots of IRD identified in 10-cm bins downcore, (d) shipboard eye counts 1 versus neural network counts, (e) shipboard eye counts 2 versus neural network counts, and (f) shipboard eye counts 1 versus shipboard eye counts 2.

eye counts on the decimeter scale. Based on these results, we argue that our CNN can efficiently identify IRD in sediment core X-ray images with a similar accuracy to humans with IRD identification expertise.

3. Results

3.1. Evaluation of Convolutional Neural Network

We trained the CNN five times with the same hyperparameters to confirm reproducibility. After each training epoch, the CNN reports four metrics on how well it is doing: training accuracy, validation accuracy, training loss, and validation loss. The training accuracy is the reported accuracy of the model on the image tiles on which it was trained. The validation accuracy is the proportion of CNN-labeled pixels that are labeled correctly compared to the image tiles on which the model was not trained. A categorical cross-entropy loss function is used to calculate the training and validation loss, and this function measures the dissimilarity between the model-labeled data and the human-labeled data. Therefore, as the validation loss decreases over the training, the trained neural network becomes more accurate. Similar to the training accuracy and validation accuracy, the training loss is based on the image tiles the model was trained on, and the validation loss is the loss value of the model on the validation image tiles. Each model run reached high levels of training accuracy (>99%) and validation accuracy (>98%, Figure 4a) and low levels of training loss (<0.022) and validation loss (<0.1; Figure 4b). The model's best run, chosen based on the highest validation accuracy, has a training accuracy of 99.35% and a validation accuracy of 98.96%. As an additional visual check, we find that the trained model identifies IRD in X-ray images with both low (Figures 4c and 4d) and high (Figures 4e and 4f) IRD densities.

We propose that this automated method is an ideal new tool to count IRD due to its demonstrated consistency and accuracy. CNN-based IRD counting also minimizes human variability in X-ray image counting style, which can occur in the field or lab over the course of large projects, and/or across multiple lab groups/researchers. We further argue that if the shape of IRD grains is similar across other sediment cores, we expect that this model could be applied to other X-ray images of deep-sea sediment cores.

In the next section, we present IRD data labeled by the trained CNN at Sites U1536–U1538. Labeling one 15-cm X-ray image takes the CNN 55 seconds, or just under 12 minutes per 1.5 m core section using an 11 GB GeForce RTX 2080 Ti GPU, which is an order of magnitude faster than similar efforts by humans. This method rapidly accelerates the processing and quantification of IRD, allowing its users to rapidly label IRD in thousands of X-ray images.

3.2. Long-Term Evolution of Antarctic Iceberg Rafting Events

Our CNN-derived IRD records from Sites U1536, U1537, and U1538 allow us to interpret trends in Antarctic iceberg rafting events in the Scotia Sea. We focus on the results from the Dove Basin drill sites, Sites U1536 and U1537 because these two sites have the most continuous sedimentary records (spliced composite sequences) through 3.3 Ma. The IRD record from Site U1538, which has IRD counts on the splice until ~430 ka and additional IRD counts to 1.2 Ma from Hole U1538A, can be found in Figure S4 in Supporting Information S1. The IRD trends at Site U1538 are consistent with the mid-to-late Pleistocene portions of the Dove Basin records, and the overall trends and fluctuations of Sites U1536 and U1537 agree through to the base of the records at 3.3 Ma.

To get from IRD counts to fluxes, we first assigned the m CCSF depth for each labeled IRD grain (≥1 mm) in the X-ray images and then interpolated the depth to the Site U1537 age model either directly (for the U1537 IRD counts) or through the correlation to the Site U1537 m CCSF depth (for Sites U1536 and U1538). After the IRD grains were assigned an age from depth, we then binned the IRD counts into 5 kyr bins for Sites U1536 and U1537 to stay within the error of the Reilly et al. (2021) magnetostratigraphic age model. We also provide 1 kyr bin resolution for Sites U1536, U1537, and U1538 for 0–1.2 Ma in Supporting Figure S4 in Supporting Information S1 since this period falls within the Weber et al. (2022) age model with lower uncertainties. To finally derive the flux, we divided the binned IRD grains by the surface area of the core half-round, which was calculated using our consistent 5.5 cm sediment core diameter. We note that the changes in sedimentation rate (generally increasing) at our sites (Figure 5a; Reilly et al., 2021; Weber et al., 2022) affect the final amplitude and variability in the IRD flux measurements (e.g., Figure 5c compared to Figure 6f).

At Sites U1536 and U1537 the lowest overall IRD fluxes occur from 3.3 to 1.8 Ma (Figures 6f and 6g). During this period, the mean IRD fluxes at Sites U1536 and U1537 are 3.36 and 3.63 grains cm^{-2} 5 kyr^{-1}, with a standard

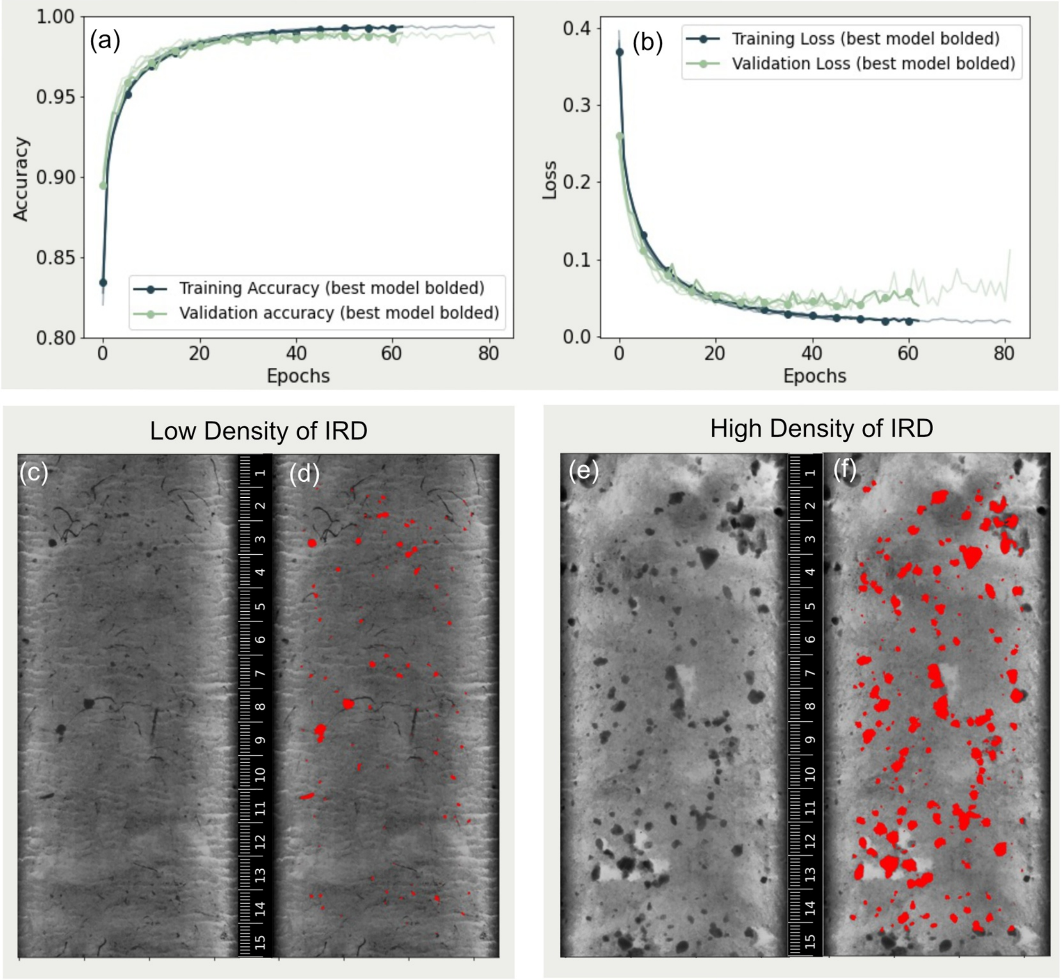

Figure 4. Convolutional neural network (CNN) training results and labeled outputs. (a) CNN training accuracy (navy) and validation accuracy (green) over the five repeat training runs. (b) CNN training loss (navy) and validation loss (green) over the five repeat training runs. (c) An example of a contrast-enhanced X-ray image with a low density of iceberg rafted debris (IRD), with the CNN-labeled output (d), where IRD grains are "labeled" in red. Panels (e) and (f) are the same as (c) and (d) however, this example image has a high density of IRD. Note, there are no labels along the edges because we only label the central 550 pixels to avoid edge effects. IRD is not labeled at the top and bottom of the image since there are overlaps between X-ray images down-core. CNN, convolutional neural network. IRD, iceberg rafted debris.

deviation of 2.76 and 2.27 grains cm^{-2} 5 kyr^{-1}, respectively. The low IRD fluxes during this period indicate a relative lack of IRD export, and therefore melting icebergs, from the Antarctic continent to the Dove Basin.

After low AIS IRD fluxes in the late Pliocene/early Pleistocene section (3.3–1.8 Ma), the flux of IRD delivered to the Scotia Sea increases after 1.8 Ma (Figures 6f and 6g). Specifically, we observe increases in both the baseline amount of IRD as well as the amplitude of multiple short-lived "major" IRD events. Between 1.8 and 0.43 Ma, the average IRD fluxes increase from 3.36 to 7.48 grains cm^{-2} 5 kyr^{-1} at Site U1536 and from 3.63 to 6.80 grains cm^{-2} 5 kyr^{-1}, at Site U1537. In addition, the standard deviation of the IRD fluxes almost doubles to 4.92 grains cm^{-2} 5 kyr^{-1} (U1536) and 4.13 grains cm^{-2} 5 kyr^{-1} (U1537). During this interval, the largest IRD fluxes often occur at the global glacial terminations, as defined by the transition of marine isotope stages in the LR04 benthic isotope stack (Lisiecki & Raymo, 2005). We discuss some possible mechanisms for this behavior below.

After 430 ka, we observe a second increase in Scotia Sea IRD fluxes. At Sites U1536, U1537, and U1538 we see average IRD fluxes increase to 16.77, 15.65, and 17.35 grains cm^{-2} 5 kyr^{-1}, respectively (Figures 6f and 6g; Figure S4d in Supporting Information S1). This increase from the pre-430 ka average IRD flux also coincides

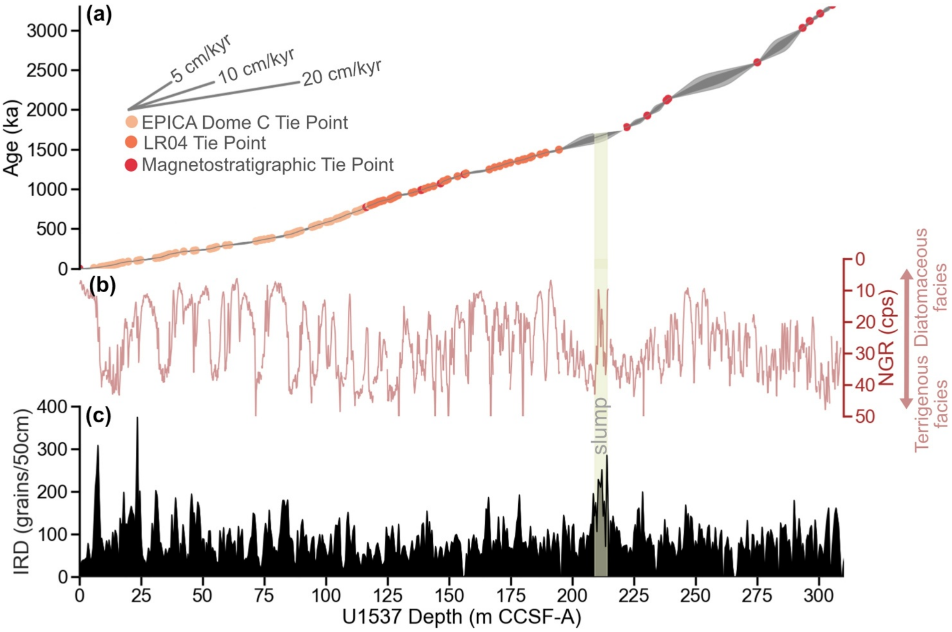

Figure 5. International Ocean Discovery Program Site U1537 data plotted on depth, before flux measurements. (a) The age/depth model used in this study with EPICA Dome C and LR04 age tie points from Weber et al. (2022) labeled in light and dark orange, respectively. Magnetostratigraphic tie points labeled in red from Reilly et al. (2021), with the 95.4% confidence interval plotted in light gray and the 68.2% confidence interval in dark gray. (b) Site U1537 NGR, note: *y*-axis is reversed. (c) IRD counts per 50 cm CCSF from Site U1537 labeled by the CNN. Light green/yellow vertical bar highlights the identified slump. NGR, natural gamma radiation. IRD, iceberg rafted debris. CNN, convolutional neural network.

with an increase in the standard deviation of the fluxes: 15.19 grains cm^{-2} 5 kyr^{-1} (U1536), 10.65 grains cm^{-2} 5 kyr^{-1} (U1537), and 12.45 grains cm^{-2} 5 kyr^{-1} (U1538). IRD fluxes are observed at glacial-interglacial transitions, including at Terminations I (14 ka), II (130 ka), IV (337 ka), and V (424 ka). The largest IRD fluxes during MIS 7/8 occur after Termination III (243 ka), at 233 and 224 ka at Site U1537 (note: slump in Site U1536 from 200 to 239 ka). In addition to the high IRD fluxes at Terminations I, II, IV, and V, there are also peak IRD fluxes after peak interglacials at 80, 92, 100, 110, 280, 300, 315, 370, 380, 395, and 415 ka (Figure S4 in Supporting Information S1). All IRD flux data from Sites U1536, U1537, and U1538 can be found in Tables S9–S13 in Supporting Information S2.

In summary, we observe two increases in our CNN-derived IRD records, after 1.8 and 0.43 Ma, which we interpret as reflecting transitions in the ice regime on the Antarctic continent over the last 3.3 Ma (Figure 6). Within the sedimentary column, these three regimes are associated with two basin-wide seismic reflectors: Reflector-a, which is dated at ~1.7 Ma, and Reflector-a', at ~0.4 Ma (Pérez et al., 2021). Given the similarity in timing between these basin-wide reflectors and the increases in IRD fluxes, we propose that the observed changes in IRD fluxes at these times are indicative of a regional ice sheet evolution, coinciding with ocean circulation changes, which are also likely contributing to the changes recorded by the seismic reflectors.

4. Discussion

4.1. Regime 1: Contracted AIS From Late Pliocene to Early Pleistocene (3.3–1.8 Ma)

The anomalously cold/high ice volume M2 glaciation occurs at 3.3 Ma, and evidence exists to suggest that during this period, the WAIS grounding line advanced along the western Ross Sea (Naish et al., 2009) and enhanced iceberg rafting at Ocean Drilling Program (ODP) Site 1165, in Prydz Bay (Figure 1a; Passchier, 2011). In addition, IRD fluxes at IODP Site U1361 (Figure 1a) off the coast of the Wilkes Subglacial Basin exhibit a shift from obliquity-paced to precession-paced IRD after ~3.5 Ma (Patterson et al., 2014). Patterson et al. (2014) suggest that during the warm Pliocene interval before ~3.5 Ma, obliquity pacing dominates the EAIS IRD record because the margin is more susceptible to oceanic forcings, and as southern high latitudes cooled, an expansion of the sea ice field occurred and therefore limited the oceanic forcing. After a condensed interval from 3.5 to 3.3 Ma,

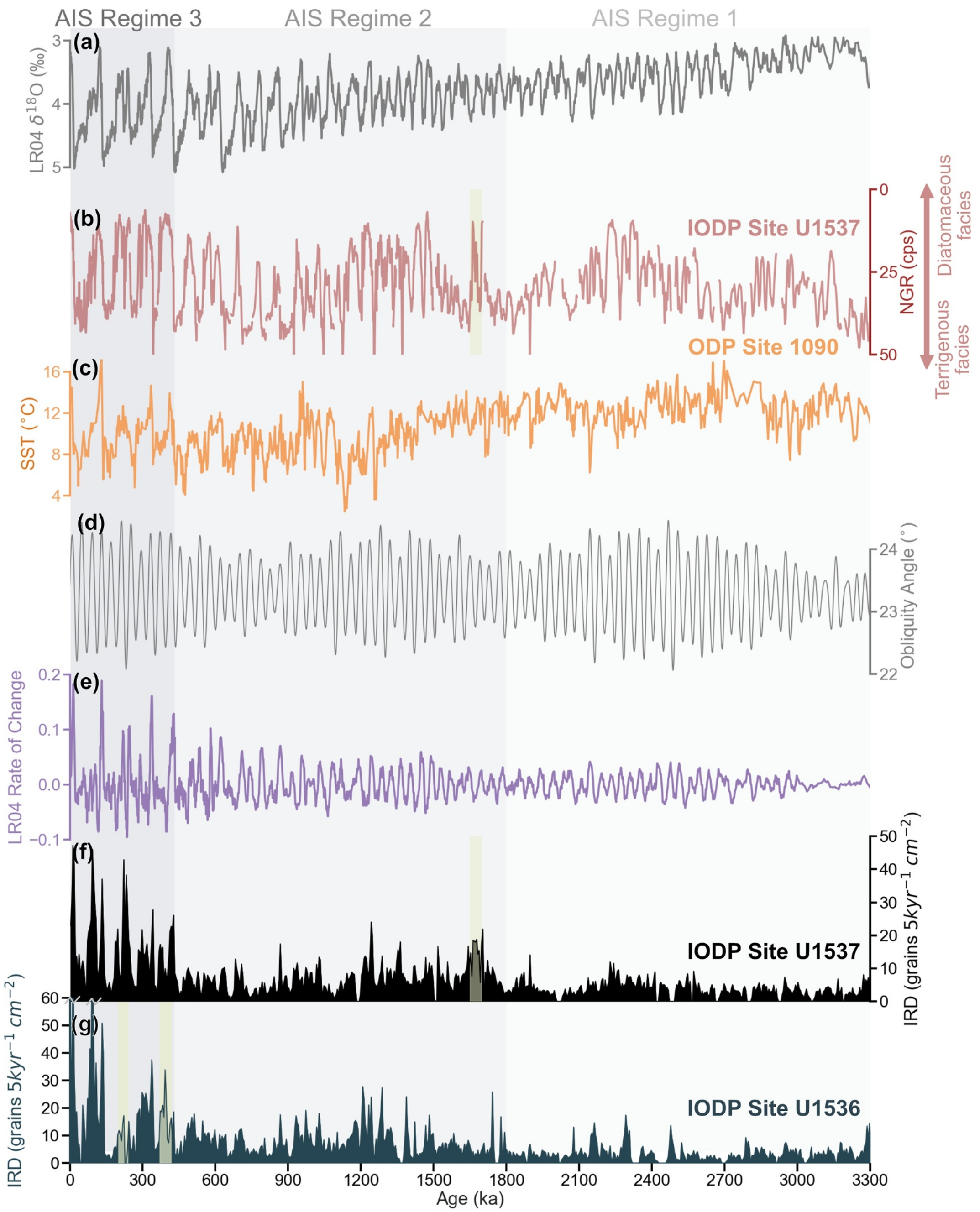

Figure 6. Major regime changes of the Antarctic Ice Sheet (AIS) over 3.3 million years. (a) The LR04 benthic δ^{18}O stack (Lisiecki & Raymo, 2005). (b) International Ocean Discovery Program (IODP) Site U1537 NGR (Weber et al., 2021). (c) Alkenone-derived SSTs from ODP Site 1090 (Martínez-Garcia et al., 2010). (d) Obliquity angle (Laskar et al., 2011). (e) LR04 rate of change with a Savitzky-Golay smoothing filter with a filter window of 9 and a polyorder of 1. (f) IODP Site U1537 and (g) Site U1536 iceberg rafted debris ($\geq$1 mm) fluxes labeled by the trained CNN, note that the fluxes are on 5 kyr binned intervals. Gray highlights indicate the three major regime changes, AIS Regime 1 (1.8–3.3 Ma), AIS Regime 2 (1.8–0.43 Ma), and AIS Regime 3 (0–0.43 Ma). Yellow highlights indicate noted slumps in IODP Sites U1536 and U1537. NGR, natural gamma radiation. SST, sea surface temperature. CNN, convolutional neural network.

the high IRD fluxes at Site U1361 correlate with summer insolation at 65°S, which they suggest represents Wilkes Subglacial Basin retreat during only peak summer insolation, which suggests that the marine margins of EAIS were less sensitive to ocean-induced melting compared to the WAIS (Patterson et al., 2014).

In the heart of Iceberg Alley in the Atlantic sector of the Southern Ocean, at IODP Sites U1536 and U1537, we find the lowest overall IRD fluxes between 3.3 and 1.8 Ma. These low IRD fluxes occur during the warmest sustained sea surface temperatures (SSTs) in the last 3.3 Ma in the sub-Antarctic Atlantic at ODP Site 1090 (42° 54.80S, 8°53.90E; Figure 1a), with average temperatures between 12 and 14°C (Figure 6c; Martínez-Garcia et al., 2010). Given that those average temperatures are comparable to the modern annual mean SSTs at Site 1090 (Figure 1 in Martínez-Garcia et al., 2010) and that satellite imagery shows iceberg discharge through Iceberg Alley today (Stuart & Long, 2011), this suggests that our IRD fluxes during this period should not be primarily affected by iceberg survivability. However, the survivability of smaller icebergs, which are more prone to melting during this time interval, is still an outstanding question and an iceberg trajectory model with realistic SSTs over this period would be valuable to provide further insights into this time period (e.g., Cook et al., 2014).

On the western Antarctic Peninsula at ODP Site 1101, Cowan et al. (2008) use IRD fluxes and sand grain microtextures to suggest that glaciers were relatively thin and had a shorter residence time at the continental shelf edge during glacial periods before 1.35 Ma. In the southern Ross Sea, lithofacies at ANDRILL site AND-1B alternate between diamictite (ice proximal) and diatomite (open marine) between 3.3 and 1.8 Ma (Naish et al., 2009; McKay, Albot, et al., 2012; McKay, Naish, et al., 2012), suggesting a highly variable AIS in the Ross Sea sector at this time. Given that Scotia Sea IRD fluxes are lowest between 3.3 and 1.8 Ma, compared to the mid-to-late Pleistocene, and the evidence for reduced and/or variable ice extent from the Ross Sea to the western Antarctic Peninsula, we hypothesize that low Scotia Sea IRD fluxes reflect a smaller AIS relative to modern. A smaller AIS may have had more terrestrial-terminating margins and a majority of the iceberg discharge may have been restricted to ice stream systems, analogous to the Ilulissat/Jakobshavn glacier and fjord system in Greenland (Enderlin et al., 2018; Sohn et al., 1998). Such a regime likely exported a fraction of the modern iceberg flux to the Scotia Sea, in contrast to the marine-terminating margins and ice shelves that characterize the late Pleistocene AIS. Thus, continuous IRD records from Sites U1536 and U1537, suggest that the expansion to sustained and sizable marine-terminating ice sheets did not occur until after 1.8 Ma.

4.2. Regime 2: AIS Expansion to Marine-Terminating Ice Sheet After 1.8 Ma

After 1.8 Ma, the increase in AIS IRD flux in the Scotia Sea coincides with Reflector-a from Pérez et al. (2021), a low-amplitude seismic reflection located in interbedded diatom ooze and silty clay in the Dove and Pirie Basins. Reflector-a was formed at an interpolated age of 1.7 Ma (interval range of 1.2–1.8 Ma), which may be associated with the onset of modern oceanic circulation in the Scotia Sea (Pérez et al., 2021). At Site U1537, Reflector-a is identified at 193 m CCSF (in Core U1537D-20F), whereas the observed slump occurs just before, from 209.5 to 214 m CCSF (in Core U1537A-22H), at ∼1.675 Ma. Therefore, we propose that this slump may be associated with a broad-scale change in ocean circulation and AIS dynamics. After 1.8 Ma, there is a marked increase in the sedimentation rate across all three Scotia Sea sites, which has been interpreted to reflect ice sheet advance and a shift to sedimentation controlled by oceanic currents instead of sediment transported from the Antarctic continental shelf (Pérez et al., 2021; Reilly et al., 2021). The observed increase in IRD flux to Iceberg Alley may indicate expansion of the AIS at this time.

In addition to a hypothesized shift in ocean circulation and dynamics interpreted within Iceberg Alley, global records of SSTs and oceanic change also suggest a major regime change after this time. SST records from ODP Site 1090 in the sub-Antarctic Atlantic show subpolar cooling from ∼1.8 to 1.2 Ma (Figure 6c; Martínez-Garcia et al., 2010). We also note that in the southern hemisphere extratropical SST stack, the long-term average cooling trend begins at ∼1.8 Ma and continues until ∼800 ka (Clark et al., 2024). In addition, Wara et al. (2005) found an increase in the zonal SST gradient, and the establishment of the Walker Circulation occurred at ∼1.7 Ma in the equatorial Pacific Ocean. Furthermore, Herbert et al. (2015) document a step-wise decrease in the Mediterranean SSTs at 1.8 Ma. Thus, many regions document a shift to overall cooler temperatures after 1.8 Ma, and indeed, this shift originally defined the base of the Pleistocene stratotype section at 1.81 Ma in Vrica, Italy (Berggren et al., 1995).

If the AIS began to transition from a primarily terrestrial-terminating ice sheet to a marine-terminating ice sheet with large fringing ice shelves at this time, we should ask whether the expansion of the Antarctic ice sheet (AIS) was in response to global cooling and/or the driver of the aforementioned global cooling. Raymo et al. (2006) proposed that long-term polar cooling driven by decreasing atmospheric CO_2 resulted in the gradual expansion of the AIS, progressively establishing the marine ice margins that characterize the entire EAIS and most of WAIS today. That study proposed that this transition began in the early Pleistocene and was largely complete by 1.0 Ma with the dozens of catchments around Antarctica, all eventually transitioning to marine-terminating sectors. Across this period, the AIS would thus have transitioned from an ice sheet where ice loss was controlled primarily by summer insolation (e.g., ablation), to an ice sheet with marine margins whose stability (calving rate) is controlled primarily by global sea level, locking the AIS ice sheet in-phase with the much larger volume of northern hemisphere ice sheet growth and decay (Raymo et al., 2006). Here our IRD data provides direct evidence of the intensification of Antarctic IRD fluxes after 1.8 Ma, which we propose reflects the increasing influence of marine-terminating ice margins in Antarctica after this time.

Given that the IRD fluxes at Sites U1536 and U1537 begin to increase after 1.8 Ma (Figure 6f), why would the AIS begin to expand at that time? While the obliquity angle has a typical 41-kyr cycle, there is also variance in the amplitude of the obliquity angle on a 1.2-Myr wavelength caused by eccentricity modulation (Figure 6d). These 1.2-Myr low-amplitude "nodes" of obliquity as well as minima in the 400 kyr-long eccentricity cycle result in a period of notably low seasonality, an orbital configuration that is favorable for ice-sheet expansion because of mild (colder) summers and mild (warmer) winters, allowing enhanced ice accumulation (in winters) to outpace ice ablation (in summers) (Pälike et al., 2006; Patterson et al., 2014; Zachos et al., 2001). At ∼1.8 Ma, a minimum in the amplitude of obliquity is associated with a 1.2-Myr node, creating an orbital configuration we propose was ideal for AIS expansion. Notably, Dove Basin physical properties (including NGR) also exhibit low variability with respect to obliquity at 1.8 Ma, with increasing variability after this time period (Figure 6b; Reilly et al., 2021).

To summarize, a minimum in long-wavelength obliquity amplitude at ∼1.8 Ma would have resulted in milder summers and winters, allowing ice accumulation to outpace ablation. Therefore, we propose that the increase in the IRD fluxes after 1.8 Ma at Sites U1536 and U1537 is the result of the AIS expanding from a primarily terrestrial-terminating to a primarily marine-terminating ice sheet. Consequently, there would have been an expansion of large marine ice shelves (e.g., The Filchner-Ronne) at this time, likely driving an enhanced volume of icebergs discharged through to Iceberg Alley following each collapse. After this point, the AIS became more sensitive to global ice sheet rhythms and global sea level, leading to enhanced in-phase behavior between AIS and northern hemisphere ice sheets.

This inferred AIS expansion to a marine-terminating ice sheet after 1.8 Ma could be the first step on a path to the Mid-Pleistocene Transition (MPT), the shift from predominantly 41–100 kyr global glacial-interglacial cycles. Specifically, our proposed expansion of the AIS prior to the MPT supports the hypothesis of Chalk et al. (2017), suggesting that an ice sheet expansion could have driven increased glacial atmospheric dustiness either directly through sea-level lowering or indirectly because of atmospheric cooling, drying, and/or changes in surface winds. Our findings also support the recent work by An et al. (2024), which shows that AIS expansion between 2 and 1.25 Ma drove the increase in Southern Ocean sea ice, driving NH moisture transport and cooling, thereby expanding NH ice sheets through the MPT. Therefore, constraining the fluxes and timing of AIS iceberg rafting events during the early-to-mid-Pleistocene is key to understanding the long-term drivers and mechanisms of the MPT.

4.3. Regime 3: Increased Deglaciation Instability After Mid-Brunhes Event (~430 ka)

Although we find evidence for an expanded AIS after 1.8 Ma, there is likely further expansion of AIS at the MIS 12 glaciation (∼430 ka) and greater AIS instability at glacial terminations after this point. This secondary increase in IRD fluxes at Sites U1536, U1537, and U1538 aligns with seismic Reflector a' (∼0.4 Ma), the uppermost stratigraphic discontinuity in the Dove and Pirie basins (Pérez et al., 2021). After Reflector a', there is a transition to higher amplitude magnetic susceptibility variability in Scotia Sea records (Pérez et al., 2021; Weber et al., 2022). In addition, after MIS 12, the interglacial periods exhibit the lowest magnetic susceptibility values over the 3.3 Ma, which Pérez et al. (2021) interpreted as either (a) limited extension of the AIS and/or (b) a higher production and outflow of Weddell Sea Deep Water during the interglacials. The higher amplitude magnetic susceptibility within the Dove Basin beginning after MIS 12 is coincident with the Mid-Brunhes Event, a period after which there are higher amplitude glacial cycles, with warmer interglacials, and higher atmospheric CO_2 values (Tzedakis et al., 2022 *and references therein*). Given the large IRD fluxes at the glacial terminations after MIS 12, we interpret these as large AIS iceberg discharges during the onset of interglacials associated with AIS retreat events. This argument is supported by evidence for enhanced inland erosion of the Wilkes Subglacial Basin at IODP Site U1361 (Figure 1a) during MIS 5, 9, and 11 (Wilson et al., 2018). Lau et al. (2023) provide further evidence for WAIS retreat and collapse at the last interglacial, just after our increase in IRD fluxes at Termination II.

The rate of change of the LR04 stack can indicate periods of rapid global mean sea level change, typically at the terminations of glacial periods (Figure 6e). Each termination from Termination IV to the present is associated with high IRD export to the Scotia Sea. This increase in IRD flux amplitude at terminations coincides with an increase in the amplitude of the LR04 rate of change after the Mid-Brunhes Event. We find that after the Mid-Brunhes Shift, each glacial termination is associated with elevated IRD fluxes, suggesting greater retreat due to enhanced instability of the marine-terminating AIS and ice shelf edge. This enhanced instability beginning at Termination V could be driven by the proposed mechanisms of marine ice-sheet instability (MISI), where marine-based ice sheets on retrograded bed slopes retreat rapidly after a perturbation from equilibrium (Favier et al., 2014; Schoof, 2007).

In addition to the major iceberg rafting events at terminations, we also observe high IRD fluxes during the late interglacials/glacial inceptions. We propose the following general overview of a glacial/interglacial cycle after the Mid-Brunhes Event: First, rapid global sea level rise at the terminations drives the marine-terminating AIS to rapidly collapse and retreat due to marine ice sheet instability, resulting in a dramatic increase in icebergs and IRD fluxes. Low IRD fluxes are found during interglacials because the now retreated AIS has ice shelves calving off large, tabular icebergs from ice shelves, "cleaned" of sediment due to basal melt from warm water now circulating over the shelf edge (Ashley & Smith, 2000; Evans & Pudsey, 2002; Pritchard et al., 2012). After the interglacial, the ice sheet expands back out to the edges of the continental margins, thus becoming less susceptible to sub-surface ice shelf ocean melting, and subsequent iceberg discharge events (i.e., driven by local insolation maxima) could deposit additional IRD to the Scotia Sea.

5. Conclusion

Constraining past iceberg rafting events is vital to understanding modern ice sheet stability and behavior in light of anthropogenic atmospheric and oceanic warming. However, quantifying IRD fluxes in physical samples can be a laborious task. Our new machine learning model identifies IRD with accuracy similar to a human eye and enables automated IRD detection consistently down-core and over millions of years. With the development of this CNN, we can quickly and accurately compare multi-million-year records of ice sheet rafting events from multiple sites within the same region, providing greater regional context for AIS instability.

Using this CNN, we find evidence for three AIS regimes over 3.3 million years based on the IRD fluxes at IODP Sites U1536–U1538 in the heart of Iceberg Alley. We interpret the low IRD flux between 3.3 and 1.8 Ma as evidence of a smaller and, perhaps, terrestrial-terminating AIS. After 1.8 Ma, an increase in the intensity and variability of IRD fluxes indicate AIS expansion at a minimum in obliquity and a shift from a primarily terrestrial-terminating to an increasingly marine-terminating AIS with expanded ice shelves, similar to the modern AIS. During this interval, cool summers and mild winters could have caused snow accumulation to outpace ablation in coastal regions, resulting in more marine-terminating AIS margins. AIS expansion after 1.8 Ma also coincides with Southern Ocean cooling. After 430 ka, we see a second increase in IRD flux, with notable maxima at glacial terminations, indicating that after the Mid-Brunhes Event, the AIS expanded further and thus became inherently more unstable, driving large and rapid collapses at glacial terminations.

This study lays the groundwork for future regional and local studies. First, the trained model and the model architecture code are open-access, and we encourage groups to use and further train this model with their own X-ray images. Second, it will be vital to determine the provenance of the IRD exported to Iceberg Alley, to determine the past sensitivity of Antarctica's ice sheets to climate on glacial/interglacial timescales, and beyond.

Conflict of Interest

The authors declare no conflicts of interest relevant to this study.

Data Availability Statement

The data tables are available on Zenodo (Jasper et al., 2024). In addition, the trained convolutional neural network and the training data can be found on Zenodo (Jasper, 2024b). *Code availability:* The code for this study can be accessed via GitHub (https://github.com/cejasper/ird-cnn) or on Zenodo (Jasper, 2024a).

Acknowledgments

We thank all of the IODP Expedition 382 shipboard scientists for their collection of shipboard data, core descriptions, and IRD eye counts on X-ray images. In addition, we are grateful to the captain, crew, and the IODP staff that made IODP Expedition 382 successful. This research used samples and data provided by IODP. This research was supported by Columbia University's Graduate School of Arts and Sciences, and CEJ is supported by the National Science Foundation Graduate Research Fellowship Program, DGE-2036197. CEJ and MER received additional support from the US Science Support Program IODP Expedition 382 Post-Expedition Award and a Columbia Climate Center grant. BR, SH, and TW received support from NSF-OPP Awards 2114763, 2114768, and 2302832. We thank Jasper Baur, Roger Creel, and Jerry McManus for their insightful feedback on the method and manuscript. In addition, we thank our two anonymous reviewers and the Associate Editor for their careful review and comments, which made this manuscript better.

References

Abadi, M., Agarwal, A., Barham, P., Brevdo, E., Chen, Z., Citro, C., et al. (2015). TensorFlow: Large-scale machine learning on heterogeneous systems. *Zenodo*. https://doi.org/10.5281/zenodo.12119782

Alley, R. B., Cuffey, K. M., Evenson, E. B., Strasser, J. C., Lawson, D. E., & Larson, G. J. (1997). How glaciers entrain and transport basal sediment: Physical constraints. *Quaternary Science Reviews*, *16*(9), 1017–1038. https://doi.org/10.1016/S0277-3791(97)00034-6

An, Z., Zhou, W., Zhang, Z., Zhang, X., Liu, Z., Sun, Y., et al. (2024). Mid-Pleistocene climate transition triggered by Antarctic Ice Sheet growth. *Science*, *385*(6708), 560–565. https://doi.org/10.1126/science.abn4861

Anderson, J. B., & Andrews, J. T. (1999). Radiocarbon constraints on ice sheet advance and retreat in the Weddell Sea, Antarctica. *Geology*, *27*(2), 179. https://doi.org/10.1130/0091-7613(1999)027<0179:RCOISA>2.3.CO;2

Andrews, J. T. (2000). Icebergs and iceberg rafted detritus (IRD) in the North Atlantic: Facts and assumptions. *Oceanography*, *13*(3), 100–108. https://doi.org/10.5670/oceanog.2000.19

Ashley, G. M., & Smith, N. D. (2000). Marine sedimentation at a calving glacier margin. *GSA Bulletin*, *112*(5), 657–667. https://doi.org/10.1130/0016-7606(2000)112<657:MSAACG>2.0.CO;2

Bailey, I., Hemming, S., Reilly, B. T., Rollinson, G., Williams, T., Weber, M. E., et al. (2022). Episodes of early Pleistocene West Antarctic ice sheet retreat recorded by iceberg alley sediments. *Paleoceanography and Paleoclimatology*, *37*(7), e2022PA004433. https://doi.org/10.1029/2022PA004433

Barker, S., Starr, A., Conn, S., Lordsmith, S., Owen, L., Nederbragt, A., et al. (2022). Persistent influence of precession on northern ice sheet variability since the early Pleistocene. *Science*, *376*(6596), 961–967. https://doi.org/10.1126/science.abm4033

Bartels, M., Titschack, J., Fahl, K., Stein, R., Seidenkrantz, M.-S., Hillaire-Marcel, C., & Hebbeln, D. (2017). Atlantic water advection vs. glacier dynamics in northern Spitsbergen since early deglaciation. *Climate of the Past*, *13*(12), 1717–1749. https://doi.org/10.5194/cp-13-1717-2017

Bazin, L., Landais, A., Lemieux-Dudon, B., Toyé Mahamadou Kele, H., Veres, D., Parrenin, F., et al. (2013). An optimized multi-proxy, multi-site Antarctic ice and gas orbital chronology (AICC2012): 120–800 ka. *Climate of the Past*, *9*(4), 1715–1731. https://doi.org/10.5194/cp-9-1715-2013

Berggren, W. A., Hilgen, F. J., Langereis, C. G., Kent, D. V., Obradovich, J. D., Raffi, I., et al. (1995). Late Neogene chronology: New perspectives in high-resolution stratigraphy. *Geological Society of America Bulletin*, *107*(11), 1272–1287. https://doi.org/10.1130/0016-7606(1995)107<1272:LNCNPI>2.3.CO;2

Cederstrøm, J. M., van der Bilt, W. G. M., Støren, E. W. N., & Rutledal, S. (2021). Semi-automatic ice-rafted debris quantification with computed tomography. *Paleoceanography and Paleoclimatology*, *36*(10), e2021PA004293. https://doi.org/10.1029/2021PA004293

Chaipornkaew, L., Elston, H., Cooke, M., Mukerji, T., & Graham, S. A. (2022). Predicting off-fault deformation from experimental strike-slip fault images using convolutional neural networks. *Geophysical Research Letters*, *49*(2), e2021GL096854. https://doi.org/10.1029/2021GL096854

Chalk, T. B., Hain, M. P., Foster, G. L., Rohling, E. J., Sexton, P. F., Badger, M. P. S., et al. (2017). Causes of ice age intensification across the Mid-Pleistocene Transition. *Proceedings of the National Academy of Sciences*, *114*(50), 13114–13119. https://doi.org/10.1073/pnas.1702143114

Chollet, F. (2015). Keras. Retrieved from https://keras.io

Clark, P. U., Shakun, J. D., Rosenthal, Y., Köhler, P., & Bartlein, P. J. (2024). Global and regional temperature change over the past 4.5 million years. *Science*, *383*(6685), 884–890. https://doi.org/10.1126/science.adi1908

Cook, C. P., Hill, D. J., van de Flierdt, T., Williams, T., Hemming, S. R., Dolan, A. M., et al. (2014). Sea surface temperature control on the distribution of far-traveled Southern Ocean ice-rafted detritus during the Pliocene. *Paleoceanography*, *29*(6), 533–548. https://doi.org/10.1002/2014PA002625

Cowan, E. A. (2001). Identification of the glacial signal from the Antarctic Peninsula since 3.0 Ma at Site 1101 in a continental rise sediment drift. *Proceedings of the Ocean Drilling Program, Scientific Results*, *178*, 1–22. https://doi.org/10.2973/odp.proc.sr.178.206.2001

Cowan, E. A., Hillenbrand, C.-D., Hassler, L. E., & Ake, M. T. (2008). Coarse-grained terrigenous sediment deposition on continental rise drifts: A record of Plio-Pleistocene glaciation on the Antarctic Peninsula. *Palaeogeography, Palaeoclimatology, Palaeoecology*, *265*(3), 275–291. https://doi.org/10.1016/j.palaeo.2008.03.010

Denton, G. H., Hughes, T. J., & Karlén, W. (1986). Global ice-sheet system interlocked by sea level. *Quaternary Research*, *26*(1), 3–26. https://doi.org/10.1016/0033-5894(86)90081-5

Diekmann, B. (2007). Sedimentary patterns in the late Quaternary Southern Ocean. *Deep Sea Research Part II: Topical Studies in Oceanography*, *54*(21), 2350–2366. https://doi.org/10.1016/j.dsr2.2007.07.025

Diekmann, B., Fütterer, D. K., Grobe, H., Hillenbrand, C. D., Kuhn, G., Michels, K., et al. (2003). Terrigenous sediment supply in the polar to temperate South Atlantic: Land-ocean Links of environmental changes during the late Quaternary. In G. Wefer, S. Mulitza, & V. Ratmeyer (Eds.), *The South Atlantic in the Late Quaternary* (pp. 375–399). Springer Berlin Heidelberg. https://doi.org/10.1007/978-3-642-18917-3_18

Dyer, B., Austermann, J., D'Andrea, W. J., Creel, R. C., Sandstrom, M. R., Cashman, M., et al. (2021). Sea-level trends across the Bahamas constrain peak last interglacial ice melt. *Proceedings of the National Academy of Sciences*, *118*(33), e2026839118. https://doi.org/10.1073/pnas.2026839118

Enderlin, E. M., Carrigan, C. J., Kochtitzky, W. H., Cuadros, A., Moon, T., & Hamilton, G. S. (2018). Greenland iceberg melt variability from high-resolution satellite observations. *The Cryosphere*, *12*(2), 565–575. https://doi.org/10.5194/tc-12-565-2018

Evans, J., & Pudsey, C. J. (2002). Sedimentation associated with Antarctic Peninsula ice shelves: Implications for palaeoenvironmental reconstructions of glacimarine sediments. *Journal of the Geological Society*, *159*(3), 233–237. https://doi.org/10.1144/0016-764901-125

Favier, L., Durand, G., Cornford, S. L., Gudmundsson, G. H., Gagliardini, O., Gillet-Chaulet, F., et al. (2014). Retreat of Pine Island Glacier controlled by marine ice-sheet instability. *Nature Climate Change*, *4*(2), 117–121. https://doi.org/10.1038/nclimate2094

Gomez, N., Weber, M. E., Clark, P. U., Mitrovica, J. X., & Han, H. K. (2020). Antarctic ice dynamics amplified by Northern Hemisphere sea-level forcing. *Nature*, *587*, 7835–8604. https://doi.org/10.1038/s41586-020-2916-2

Grobe, H. (1987). A simple method for the determination of ice-rafted debris in sediment cores. *Polarforschung*, *57*(3), 123–126.

Habib, P., Alsamman, A., Hassanein, S., & Hamwieh, A. (2020). Developing convolutional neural networks-based system for Predicting Pneumonia using X-radiography image. In *Highlights in bioscience* (pp. 1–3). https://doi.org/10.36462/H.BioSci.20201

Hays, J. D., Imbrie, J., & Shackleton, N. J. (1976). Variations in the Earth's orbit: Pacemaker of the ice ages. *Science*, *194*(4270), 1121–1132. https://doi.org/10.1126/science.194.4270.1121

Herbert, T. D., Ng, G., & Cleaveland Peterson, L. (2015). Evolution of Mediterranean sea surface temperatures 3.5–1.5 Ma: Regional and hemispheric influences. *Earth and Planetary Science Letters*, *409*, 307–318. https://doi.org/10.1016/j.epsl.2014.10.006

Hodell, D. A., Crowhurst, S. J., Lourens, L., Margari, V., Nicolson, J., Rolfe, J. E., et al. (2023). A 1.5-million-year record of orbital and millennial climate variability in the North Atlantic. *Climate of the Past*, *19*(3), 607–636. https://doi.org/10.5194/cp-19-607-2023

Huang, H., Gutjahr, M., Eisenhauer, A., & Kuhn, G. (2020). No detectable Weddell Sea Antarctic bottom water export during the last and penultimate glacial maximum. *Nature Communications*, *11*(1), 424. https://doi.org/10.1038/s41467-020-14302-3

Jasper, C. (2024a). cejasper/ird-cnn: First release of IRD CNN for Zenodo archive (v1.0.0) [Software]. *Zenodo*. https://doi.org/10.5281/zenodo.13333916

Jasper, C. (2024b). Training data and trained convolutional neural network model for "A 3.3-million-year record of Antarctic iceberg rafted debris and ice sheet evolution quantified by machine learning". [Model]. *Zenodo*. https://doi.org/10.5281/zenodo.13333689

Jasper, C., Dyer, B., Reilly, B., Williams, T., Hemming, S., & Raymo, M. (2024). Supplementary tables for "A 3.3-million-year record of Antarctic iceberg rafted debris and ice sheet evolution quantified by machine learning" [Dataset]. *Zenodo*. https://doi.org/10.5281/zenodo.13328432

Keany, J., Ledbetter, M., Watkins, N., & Huang, T.-C. (1976). Diachronous deposition of ice-rafted debris in sub-Antarctic deep-sea sediments. *Geological Society of America Bulletin*, *87*(6), 873. https://doi.org/10.1130/0016-7606(1976)87<873:DDOIDI>2.0.CO;2

Krizhevsky, A., Sutskever, I., & Hinton, G. E. (2012). ImageNet classification with deep convolutional neural networks. In *Advances in neural information processing systems* (Vol. 25). Retrieved from https://proceedings.neurips.cc/paper/2012/hash/c399862d3b9d6b76c8436e924a68c45b-Abstract.html

Lai, C.-Y., Kingslake, J., Wearing, M. G., Chen, P.-H. C., Gentine, P., Li, H., et al. (2020). Vulnerability of Antarctica's ice shelves to meltwater-driven fracture. *Nature*, *584*, 7822–8578. https://doi.org/10.1038/s41586-020-2627-8

Laskar, J., Fienga, A., Gastineau, M., & Manche, H. (2011). La2010: A new orbital solution for the long-term motion of the Earth. *Astronomy & Astrophysics*, *532*, A89. https://doi.org/10.1051/0004-6361/201116836

Lau, S. C. Y., Wilson, N. G., Golledge, N. R., Naish, T. R., Watts, P. C., Silva, C. N. S., et al. (2023). Genomic evidence for West Antarctic ice sheet collapse during the last interglacial. *Science*, *382*(6677), 1384–1389. https://doi.org/10.1126/science.ade0664

LeCun, Y., Kavukcuoglu, K., & Farabet, C. (2010). Convolutional networks and applications in vision. In *Proceedings of 2010 IEEE International Symposium on Circuits and systems* (pp. 253–256). https://doi.org/10.1109/ISCAS.2010.5537907

Lisiecki, L. E., & Raymo, M. E. (2005). A Pliocene-Pleistocene stack of 57 globally distributed benthic δ^{18}O records. *Paleoceanography*, *20*(1), PA1003. https://doi.org/10.1029/2004PA001071

Lougheed, B. C., & Obrochta, S. P. (2019). A rapid, deterministic age-depth modeling routine for geological sequences with inherent depth uncertainty. *Paleoceanography and Paleoclimatology*, *34*(1), 122–133. https://doi.org/10.1029/2018PA003457

Maldonado, A., Barnolas, A., Bohoyo, F., Galindo-Zaldívar, J., Hernández-Molina, J., Lobo, F., et al. (2003). Contourite deposits in the central Scotia Sea: The importance of the Antarctic circumpolar current and the Weddell Gyre flows. *Palaeogeography, Palaeoclimatology, Palaeoecology*, *198*(1–2), 187–221. https://doi.org/10.1016/S0031-0182(03)00401-2

Marchant, R., Tetard, M., Pratiwi, A., Adebayo, M., & de Garidel-Thoron, T. (2020). Automated analysis of foraminifera fossil records by image classification using a convolutional neural network. *Journal of Micropalaeontology*, *39*(2), 183–202. https://doi.org/10.5194/jm-39-183-2020

Martínez-Garcia, A., Rosell-Melé, A., McClymont, E. L., Gersonde, R., & Haug, G. H. (2010). Subpolar Link to the emergence of the modern equatorial Pacific cold Tongue. *Science*, *328*(5985), 1550–1553. https://doi.org/10.1126/science.1184480

McKay, R., Albot, O., Dunbar, G. B., Lee, J. I., Lee, M. K., Yoo, K.-C., et al. (2022). A comparison of methods for identifying and quantifying ice rafted debris on the Antarctic margin. *Paleoceanography and Paleoclimatology*, *37*(4), e2021PA004404. https://doi.org/10.1029/2021PA004404

McKay, R., Naish, T., Carter, L., Riesselman, C., Dunbar, R., Sjunneskog, C., et al. (2012). Antarctic and Southern Ocean influences on late Pliocene global cooling. *Proceedings of the National Academy of Sciences*, *109*(17), 6423–6428. https://doi.org/10.1073/pnas.1112248109

McKay, R., Naish, T., Powell, R., Barrett, P., Scherer, R., Talarico, F., et al. (2012). Pleistocene variability of Antarctic ice sheet extent in the Ross embayment. *Quaternary Science Reviews*, *34*, 93–112. https://doi.org/10.1016/j.quascirev.2011.12.012

McManus, J. F., Oppo, D. W., & Cullen, J. L. (1999). A 0.5-million-year record of millennial-scale climate variability in the North Atlantic. *Science*, *283*(5404), 971–975. https://doi.org/10.1126/science.283.5404.971

Naish, T., Powell, R., Levy, R., Wilson, G., Scherer, R., Talarico, F., et al. (2009). Obliquity-paced Pliocene West Antarctic ice sheet oscillations. *Nature*, *458*, 7236–7328. https://doi.org/10.1038/nature07867

Naveira Garabato, A. C., McDonagh, E. L., Stevens, D. P., Heywood, K. J., & Sanders, R. J. (2002). On the export of Antarctic bottom water from the Weddell Sea. *Deep Sea Research Part II: Topical Studies in Oceanography*, *49*(21), 4715–4742. https://doi.org/10.1016/S0967-0645(02)00156-X

Pälike, H., Norris, R. D., Herrle, J. O., Wilson, P. A., Coxall, H. K., Lear, C. H., et al. (2006). The heartbeat of the Oligocene climate system. *Science*, *314*(5807), 1894–1898. https://doi.org/10.1126/science.1133822

Passchier, S. (2011). Linkages between east Antarctic ice sheet extent and Southern Ocean temperatures based on a Pliocene high-resolution record of ice-rafted debris off Prydz Bay, east Antarctica. *Paleoceanography*, *26*(4), PA4204. https://doi.org/10.1029/2010PA002061

Patterson, M. O., McKay, R., Naish, T., Escutia, C., Jimenez-Espejo, F. J., Raymo, M. E., et al. (2014). Orbital forcing of the East Antarctic ice sheet during the Pliocene and early Pleistocene. *Nature Geoscience*, *7*, 11–847. https://doi.org/10.1038/ngeo2273

Pérez, L. F., Martos, Y. M., García, M., Weber, M. E., Raymo, M. E., Williams, T., et al. (2021). Miocene to present oceanographic variability in the Scotia Sea and Antarctic ice sheets dynamics: Insight from revised seismic-stratigraphy following IODP Expedition 382. *Earth and Planetary Science Letters*, *553*, 116657. https://doi.org/10.1016/j.epsl.2020.116657

Pritchard, H., Ligtenberg, S., Fricker, H., Vaughan, D., Van den Broeke, M., & Padman, L. (2012). Antarctic ice-sheet loss driven by basal melting of ice shelves. *Nature*, *484*(7395), 502–505. https://doi.org/10.1038/nature10968

Rackow, T., Wesche, C., Timmermann, R., Hellmer, H. H., Juricke, S., & Jung, T. (2017). A simulation of small to giant Antarctic iceberg evolution: Differential impact on climatology estimates. *Journal of Geophysical Research: Oceans*, *122*(4), 3170–3190. https://doi.org/10.1002/2016JC012513

Raymo, M. E., Lisiecki, L. E., & Nisancioglu, K. H. (2006). Plio-pleistocene ice volume, Antarctic climate, and the global δ^{18}O record. *Science*, *313*(5786), 492–495. https://doi.org/10.1126/science.1123296

Raymo, M. E., Ruddiman, W., & Clement, B. (1986). Pliocene-Pleistocene paleoceanography of the North-Atlantic at deep-sea drilling project site-609. In *Initial reports of the deep sea drilling project* (Vol. 94, pp. 895–901).

Reilly, B. T., Stoner, J. S., Mix, A. C., Walczak, M. H., Jennings, A., Jakobsson, M., et al. (2019). Holocene break-up and reestablishment of the Petermann ice Tongue, northwest Greenland. *Quaternary Science Reviews*, *218*, 322–342. https://doi.org/10.1016/j.quascirev.2019.06.023

Reilly, B. T., Tauxe, L., Brachfeld, S., Raymo, M., Bailey, I., Hemming, S., et al. (2021). New magnetostratigraphic insights from iceberg Alley on the rhythms of Antarctic climate during the Plio-Pleistocene. *Paleoceanography and Paleoclimatology*, *36*(2), e2020PA003994. https://doi.org/10.1029/2020PA003994

Ruddiman, W. F. (1977). Late Quaternary deposition of ice-rafted sand in the subpolar North Atlantic (lat 40° to 65°N). *GSA Bulletin*, *88*(12), 1813–1827. https://doi.org/10.1130/0016-7606(1977)88<1813:LQDOIS>2.0.CO;2

Schoof, C. (2007). Ice sheet grounding line dynamics: Steady states, stability, and hysteresis. *Journal of Geophysical Research*, *112*(F3), F03S28. https://doi.org/10.1029/2006JF000664

Silva, T. A. M., Bigg, G. R., & Nicholls, K. W. (2006). Contribution of giant icebergs to the Southern Ocean freshwater flux. *Journal of Geophysical Research*, *111*(C3), C03004. https://doi.org/10.1029/2004JC002843

Sohn, H.-G., Jezek, K. C., & van der Veen, C. J. (1998). Jakobshavn Glacier, west Greenland: 30 years of spaceborne observations. *Geophysical Research Letters*, *25*(14), 2699–2702. https://doi.org/10.1029/98GL01973

Starr, A., Hall, I. R., Barker, S., Rackow, T., Zhang, X., Hemming, S. R., et al. (2021). Antarctic icebergs reorganize ocean circulation during Pleistocene glacials. *Nature*, *589*, 7841–8241. https://doi.org/10.1038/s41586-020-03094-7

Stuart, K. M., & Long, D. G. (2011). Tracking large tabular icebergs using the SeaWinds Ku-band microwave scatterometer. *Deep Sea Research Part II: Topical Studies in Oceanography*, *58*(11), 1285–1300. https://doi.org/10.1016/j.dsr2.2010.11.004

Tapley, B. D., Watkins, M. M., Flechtner, F., Reigber, C., Bettadpur, S., Rodell, M., et al. (2019). Contributions of GRACE to understanding climate change. *Nature Climate Change*, *9*, 5–369. https://doi.org/10.1038/s41558-019-0456-2

Teitler, L., Warnke, D. A., Venz, K. A., Hodell, D. A., Becquey, S., Gersonde, R., & Teitler, W. (2010). Determination of Antarctic Ice Sheet stability over the last ~500 ka through a study of iceberg-rafted debris. *Paleoceanography*, *25*(1), PA1202. https://doi.org/10.1029/2008PA001691

Tzedakis, P. C., Hodell, D. A., Nehrbass-Ahles, C., Mitsui, T., & Wolff, E. W. (2022). Marine isotope stage 11c: An unusual interglacial. *Quaternary Science Reviews*, *284*, 107493. https://doi.org/10.1016/j.quascirev.2022.107493

van der Walt, S., Schönberger, J. L., Nunez-Iglesias, J., Boulogne, F., Warner, J. D., Yager, N., et al. (2014). scikit-image: Image processing in Python. *PeerJ*, *2*, e453. https://doi.org/10.7717/peerj.453

Wang, L., Lin, Z. Q., & Wong, A. (2020). COVID-net: A tailored deep convolutional neural network design for detection of COVID-19 cases from chest X-ray images. *Scientific Reports*, *10*(1), 19549. https://doi.org/10.1038/s41598-020-76550-z

Wara, M. W., Ravelo, A. C., & Delaney, M. L. (2005). Permanent El Niño-like Conditions during the Pliocene warm period. *Science*, *309*(5735), 758–761. https://doi.org/10.1126/science.1112596

Weber, M. E., Bailey, I., Hemming, S. R., Martos, Y. M., Reilly, B. T., Ronge, T. A., et al. (2022). Antiphased dust deposition and productivity in the Antarctic Zone over 1.5 million years. *Nature Communications*, *13*(1), 2044. https://doi.org/10.1038/s41467-022-29642-5

Weber, M. E., Clark, P. U., Kuhn, G., Timmermann, A., Sprenk, D., Gladstone, R., et al. (2014). Millennial-scale variability in Antarctic ice-sheet discharge during the last deglaciation. *Nature*, *510*(7503), 134–138. https://doi.org/10.1038/nature13397

Weber, M. E., Raymo, M. E., Peck, V. L., Williams, T., & the Expedition 382 Scientists. (2019). *Expedition 382 Preliminary report: Iceberg Alley and Subantarctic ice and ocean dynamics* (Vol. 382). International Ocean Discovery Program. https://doi.org/10.14379/iodp.pr.382.2019

Weber, M. E., Raymo, M. E., Peck, V. L., Williams, T., & the Expedition 382 Scientists. (2021). *Volume 382: Iceberg Alley and Subantarctic ice and ocean dynamics (expedition 382 scientists, Ed.)* (382). International Ocean Discovery Program. https://doi.org/10.14379/iodp.proc.382.2021

Williams, T., van de Flierdt, T., Hemming, S. R., Chung, E., Roy, M., & Goldstein, S. L. (2010). Evidence for iceberg armadas from east Antarctica in the Southern Ocean during the late Miocene and early Pliocene. *Earth and Planetary Science Letters*, *290*(3), 351–361. https://doi.org/10.1016/j.epsl.2009.12.031

Wilson, D. J., Bertram, R. A., Needham, E. F., van de Flierdt, T., Welsh, K. J., McKay, R. M., et al. (2018). Ice loss from the East Antarctic ice sheet during late Pleistocene interglacials. *Nature*, *561*, 7723–8386. https://doi.org/10.1038/s41586-018-0501-8

Zachos, J. C., Shackleton, N. J., Revenaugh, J. S., Pälike, H., & Flower, B. P. (2001). Climate response to orbital forcing across the Oligocene-Miocene Boundary. *Science*, *292*(5515), 274–278. https://doi.org/10.1126/science.1058288

References From the Supporting Information

Agarap, A. F. (2019). Deep learning using rectified linear Units (ReLU) (arXiv:1803.08375). *arXiv*. https://doi.org/10.48550/arXiv.1803.08375

Kingma, D. P., & Ba, J. (2017). Adam: A method for stochastic optimization (arXiv:1412.6980). *arXiv*. https://doi.org/10.48550/arXiv.1412.6980

O'Shea, K., & Nash, R. (2015). An introduction to convolutional neural networks (arXiv:1511.08458). *arXiv*. Retrieved from http://arxiv.org/abs/1511.08458

Sharma, S., Sharma, S., & Athaiya, A. (2020). Activation functions in neural networks. *International Journal of Engineering Applied Sciences and Technology*, *04*(12), 310–316. https://doi.org/10.33564/IJEAST.2020.v04i12.054

Srivastava, N., Hinton, G., Krizhevsky, A., Sutskever, I., & Salakhutdinov, R. (2014). Dropout: A simple way to prevent neural networks from overfitting. *Journal of Machine Learning Research*, *15*(1), 1929–1958.